NANO LETTERS

Letter

pubs.acs.org/NanoLett

Direct Observation of Spatially Heterogeneous Single-Layer Graphene Oxide Reduction Kinetics

Matthew P. McDonald,[†] Ahmed Eltom,[‡] Felix Vietmeyer,[†] Janak Thapa,[§] Yurii V. Morozov,[∥] Denis A. Sokolov,[†] Jose H. Hodak,[⊥] Kizhanipuram Vinodgopal,[#] Prashant V. Kamat,[†] and Masaru Kuno*[,†]

[†]Department of Chemistry and Biochemistry, University of Notre Dame, Notre Dame, Indiana 46556, United States

[‡]Nanotechnology Engineering, University of Waterloo, Waterloo, Ontario, N2L 3G1, Canada

[§]Department of Physics, Illinois Wesleyan University, Bloomington, Illinois 61701, United States

[∥]Department of Physics, Taras Shevchenko National University of Kiev, Kiev, Ukraine

[⊥]INQUIMAE-Departamento de Química Inorgánica, Analítica y Química Físca, Facultad de Ciencias Exactas y Naturales, University of Buenos Aires, Buenos Aires, Argentina

[#]Department of Chemistry, North Carolina Central University, Durham, North Carolina 27707, United States

Supporting Information

ABSTRACT: Graphene oxide (GO) is an important precursor in the production of chemically derived graphene. During reduction, GO's electrical conductivity and band gap change gradually. Doping and chemical functionalization are also possible, illustrating GO's immense potential in creating functional devices through control of its local hybridization. Here we show that laser-induced photolysis controllably reduces individual single-layer GO sheets. The reaction can be followed in real time through sizable decreases in GO's photoluminescence efficiency along with spectral blueshifts. As-produced reduced graphene oxide (rGO) sheets undergo additional photolysis, characterized by dramatic emission enhancements and spectral redshifts. Both GO's reduction and subsequent conversion to photobrightened rGO are captured through movies of their photoluminescence kinetics. Rate maps illustrate sizable spatial and temporal heterogeneities in sp^2 domain growth and reveal how reduction "flows" across GO and rGO sheets. The observed heterogeneous reduction kinetics provides mechanistic insight into GO's conversion to chemically derived graphene and highlights opportunities for overcoming its dynamic, chemical disorder.

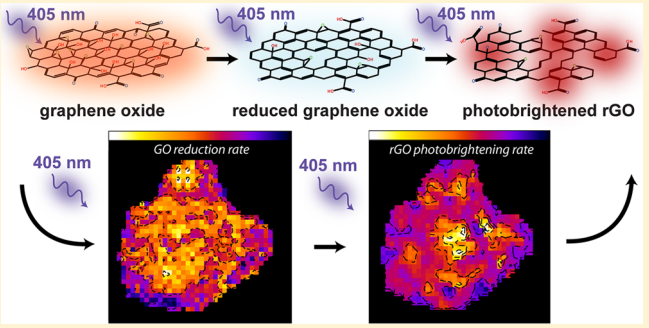

KEYWORDS: *Graphene oxide, reduced graphene oxide, photolysis, reduction, photobrightening, fluorescence intermittency*

In the search for two-dimensional (2D) systems beyond graphene, graphene oxide (GO) and reduced graphene oxide (rGO) have emerged as alternate materials. While graphene itself has attracted significant interest as a platform for observing fundamental physics such as quantum electrodynamic effects,[1] the room temperature quantum Hall effect,[2] and the Klein paradox,[3] its use in next generation electronics and renewable energy applications[4] has been hindered by the absence of a bandgap. This has subsequently spurred a desire to explore the properties of alternate 2D systems where their underlying optical and electrical properties can be better controlled and harnessed.

Graphene analogues such as GO and rGO are attractive materials in this regard. They possess sizable band gaps,[5,6] exhibit large carrier mobilities,[7,8] and emit light across the visible/near-infrared regions.[6,9] Their synthesis involves low-cost solution chemistries that result in scalable and solution-processable materials. More importantly, the ability to control GO's local conjugation and hence its electronic structure represents an exciting opportunity to chemically tailor the optical and electrical properties of a 2D system via sp^3–sp^2 interconversion.

Known methods for GO reduction include chemical,[10−13] thermal,[14−16] and photoreduction approaches.[17−21] All lead to chemical disorder, stemming from the presence of oxygen containing functionalities within GO. Specifically, carbonyl (C═O), carboxyl (COOH), hydroxyl (OH), and epoxide (C−O−C) moieties exist; OH and epoxide groups dominate GO's basal plane, while edges are primarily decorated with carbonyls and carboxyls.[22,23] The reduction of GO to rGO entails

Received: June 6, 2013
Revised: November 13, 2013

   dx.doi.org/10.1021/nl402057j | *Nano Lett.* XXXX, XXX, XXX−XXX

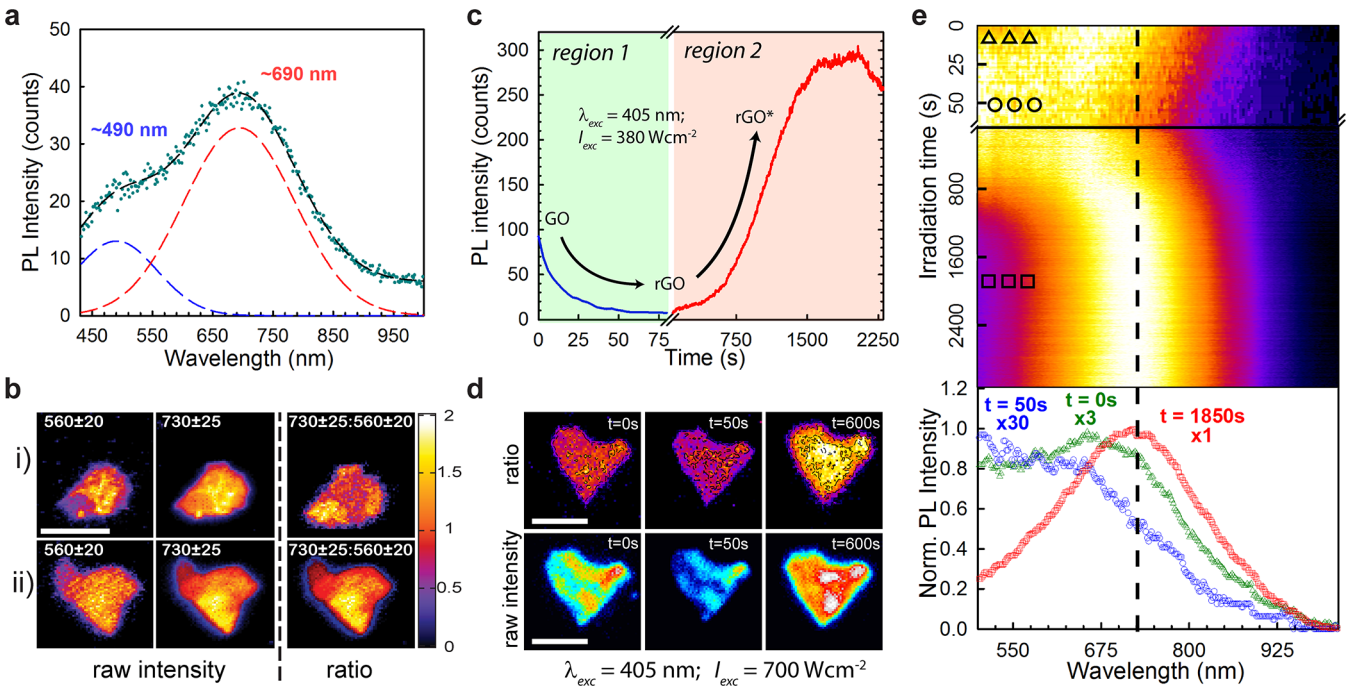

Figure 1. Emission properties of single-layer GO sheets. (a) PL spectrum of a single GO sheet (solid green circles) showing both blue and red components. The trace is fit to a sum of Gaussians (dashed black line) where two individual components (dashed blue and red lines) are extracted with center wavelengths of ~490 nm and ~690 nm. (b) Green and red emission maps of two different (i and ii) GO sheets before significant irradiation, along with their corresponding ratio maps (730 ± 25 nm/560 ± 20 nm). (c) PL intensity of a single GO sheet under continuous 405 nm laser irradiation (I_{exc} = 380 W cm^{-2}). (d) Ratio maps of individual GO sheets at different irradiation times (λ_{exc} = 405 nm; I_{exc} = 700 W cm^{-2}) constructed using the red (730 ± 25 nm) and green (560 ± 20 nm) portions of their PL spectra (top row). The bottom row shows corresponding widefield emission images. (e) Evolution of a single GO sheet's PL spectrum under continuous 405 nm laser irradiation (I_{exc} = 380 W cm^{-2}). A waterfall plot is constructed from normalized PL spectra to clearly show spectral changes during irradiation (the dashed black line is a guide for the eye). Selected regions along the time trace (marked by open symbols) are shown in the bottom panel. Scale bars: 5 μm.

removing these species, leading to ~30% C losses due to the release of CO, CO_2, H_2O, and O_2.[24] Irrespective of production method, incomplete reduction leaves behind residual oxygen bearing species and defects which suppress GO's electrical conductivity relative to graphene. A need therefore exists to better understand GO's reduction chemistry which will enable future manufacturing technologies that will allow for its controlled and/or complete reduction.

We report, for the first time, the direct observation of photolytic GO reduction, its heterogeneous intrasheet kinetics, and mechanistic aspects of GO-to-rGO interconversion. We detail correlations between the spatial location of where GO's reduction begins and rationalize the origin of its spatially heterogeneous chemistry.

Graphene oxide was prepared using a modified Hummers synthesis.[25] Resulting GO sheets possess typical dimensions of ~5 × 5 μm, as determined by transmission electron microscopy (TEM) (Supplementary Figure S1). The oxygen content of samples was determined using X-ray photoelectron spectroscopy (XPS), which yields typical carbon−carbon/carbon−oxygen bond ratios (C:O) of ~0.85 (Supplementary Figure S2). GO sheets were subsequently drop-cast onto fused silica coverslips from dilute ethanol suspensions and were examined using a home-built single molecule imaging microscope. A protocol to identify individual sheets was established by conducting control experiments on identically prepared samples using contrast differences on SiO_2 as well as the fluorescence quenching of fluorescein (Supplementary Figures S3−S4).[26] Experimental details can be found in Methods and in the Supporting Information.

On exciting samples with 405 nm light (3.06 eV), we observe that individual GO sheets fluoresce. A representative photoluminescence (PL) spectrum integrated over an entire sheet is shown in Figure 1a and resembles those previously reported in the literature.[9,27,28] Namely, a broad peak having a center wavelength of ~690 nm (1.80 eV) exists, along with a higher energy shoulder at ~490 nm (2.53 eV). While the exact origin of the broad PL has been (and continues to be) debated—for example, GO's PL has recently been assigned to sp^2 domain size distributions or to the emission of related quasi-molecular ligand/sp^2 states[9,29]—recent studies implicate heterogeneous carrier relaxation kinetics rather than confinement effects as the dominant source of broadened PL.[27]

At the single sheet level, we find a high degree of spectral heterogeneity. Emission maps of individual GO sheets [excitation wavelength (λ_{exc}) = 405 nm, excitation intensity (I_{exc}) = 150 W cm^{-2}], constructed using the ratio of their red and green PL intensities (Figure 1b), reveal significant spectral as well as spatial heterogeneities. In particular, a beamsplitter/bandpass-filter pair separates the GO PL spectrum into red (730 ± 25 nm) and green (560 ± 20 nm) channels and detects them using two separate avalanche photodiodes. The data is subsequently compiled into a single ratio map (730 ± 25 nm/560 ± 20 nm). From these images, a sizable range of emission peak positions exist as seen through the presence of bright and dim domains. For example, Figure 1b(i) shows a GO sheet with a large (~1 μm^2) portion emitting primarily red light (bottom left of sheet); the rest of the sheet emits primarily green. A similar trend can be seen in Figure 1b(ii), which again shows distinct red and green regions. Neither exhibits specific trends

dx.doi.org/10.1021/nl402057j | Nano Lett. XXXX, XXX, XXX−XXX

in their intrasheet positions (e.g., at the edge or center), having seemingly random placements. The ratio maps thus qualitatively illustrate the large intrasheet spectral heterogeneities present and the likely existence of sizable domain size distributions in GO. Analogous spatial and spectral heterogeneities are observed with other red/blue wavelength ratios (Supplementary Figure S5).

GO's photophysical properties evolve when individual sheets are exposed to 405 nm laser radiation (continuous wave, I_{exc}~380 W cm^{-2}). Initially, GO's photoluminescence quenches almost immediately (region 1, Figure 1c), where the intensity decreases by an order of magnitude over the course of ~50 s (total photon dose ~ 3.9 × 10^{22} photons/cm^2, Figure 1c, solid blue line). The corresponding quantum yield (QY) changes from 0.9% to 0.08% (Supplementary Discussion S1). Under even longer exposure times (hundreds of seconds, region 2, Figure 1c), a *photobrightening* effect is observed, with a ~3× enhancement of the original emission intensity (Figure 1c, solid red line). Resulting integrated QYs are ~3%. Both the quenching and the photobrightening are observed in all single layer specimens studied.

Intrasheet spectral heterogeneities are also dynamic. We observe that they evolve throughout the quenching/photobrightening process. This is demonstrated in Figure 1d by correlating a single sheet's red−green ratio map (top row) to its raw intensity image (bottom row) at different intervals of illumination (λ_{exc} = 405 nm; I_{exc} = 700 W cm^{-2}). These measurements highlight the following trends: (a) red−green ratios decrease over the first 50 s of illumination (region 1), (b) they increase during photobrightening in region 2, (c) the quenching/photobrightening kinetics are spatially nonuniform, and (d) predominantly red-emitting regions are the first to photobrighten (determining whether or not red-emitting regions are first to quench in region 1 is beyond the experiment's current capabilities as the quenching occurs very quickly). Apart from revealing a sheet's spatial, temporal, and spectral evolution throughout the quenching/photobrightening process, these measurements generally illustrate that GO's response in region 1 (region 2) is characterized by a spectral blueshift (redshift).

This spectral evolution is better captured through waterfall plots of a given sheet's normalized PL spectrum as a function of illumination time. Figure 1e shows data from the same specimen featured in Figure 1c and clearly reveals an initial blueshift on illumination (region 1). Upon continued illumination, the sheet's spectrum redshifts until it settles at ~725 nm (region 2). The bottom panel of Figure 1e shows normalized spectra taken at different times (t = 0, t = 50, t = 1850 s), illustrating this.

We attribute both the quenching and blueshift in region 1 to sp^2 domain growth resulting from GO photoreduction.[27,28] Namely, an increase in graphenic domain size leads to a decrease of the sample's emission QY along with a concomitant blueshift of its spectrum. Both stem from an increase in nonradiative recombination rates experienced by photogenerated carriers within an extended/interconnected sp^2 network.[27] This claim is also qualitatively consistent with the behavior of rGO and monolayer graphene, which exhibit vanishingly small photoluminescence efficiencies.[30]

The hypothesis is further supported by ensemble optical measurements where irradiating a GO suspension (λ_{exc} = 405 nm, I_{exc} = 0.2 W cm^{-2}) over the course of 16.5 h (the corresponding photon dose ~2.4 × 10^{22} photons/cm^2 places this in region 1) causes its appearance to gradually turn from light brown to black. Acquired absorption spectra reveal linear growth of the absorption as a function of irradiation time, which obscures the only visible nπ* transition at 290 nm (Supplementary Figure S6). This is in good agreement with prior literature reports about GO's reduction.[5,11]

Associating region 1 with GO photoreduction is additionally supported by three control measurements. Namely, following 405 nm illumination (16.5 h, I_{exc} = 0.2 W cm^{-2}), ensemble XPS measurements show an increase of the C:O ratio from 0.85 to 1.7. Fits to the data reveal a decrease of C−O (primarily OH and C−O−C groups) and C═O contributions to the total C1s spectrum, 46% to 33% in the former case and 5.9% to 3.4% in the latter (Supplementary Figure S2). Ensemble Fourier transform infrared (FTIR) spectroscopy shows a similar trend in functional group dissociation, where hydroxyls are the first to dissociate, followed by epoxides and then carbonyls/carboxyls (Supplementary Figure S7). In parallel, postillumination (ensemble) two probe transport measurements indicate sizable decreases of GO's sheet resistance from 1.2 × 10^{13} Ω sq^{-1} to 1.8 × 10^{11} Ω sq^{-1}, again consistent with prior ensemble transport measurements (Supplementary Figure S8).[31] All of the above single and ensemble studies thus confirm the photoreduction of GO, which, at the single sheet level, is characterized by a marked quenching and spectral blueshift (region 1).

Having correlated the initial emission quenching/blueshift with GO photoreduction, we now rationalize the brightening/redshift observed in region 2. We speculate that during this phase, extended sp^2 domains originally created within region 1 continue to expand but, more importantly, are revealed by an increase of their emission QY. What results is a photobrightened version of rGO which we term rGO*. In this regard, we suggest that a delayed physical process exists following reduction that suppresses the fast nonradiative channels that characterize photogenerated carrier dynamics in an extended/interconnected sp^2 network.[27] This causes the emission associated with individual sp^2 domains to become more apparent. Similar emission enhancements have previously been observed during the chemical reduction of GO thin film ensembles.[32] However, these films possess a PL spectrum centered at ~390 nm, which does not shift on reduction. This difference likely stems from enrichment of investigated GO ensembles with blue-emitting species through selective purification procedures.[32]

Associating red emission to photoreduced sp^2 domains is reasonable since increasing the number of aromatic rings in a functionalized sp^2 cluster readily results in an energy gap in the visible region.[28] Configuration interaction (CI) calculations[33] likewise show that energy gaps of carboxyl-functionalized sp^2 clusters lie between ~600 and ~800 nm (Supplementary Figure S9).

The hypothesis is further corroborated by single sheet Raman measurements conducted on both GO and rGO*. Specifically, we find that rGO*'s G band full-width at half-maximum (fwhm) is smaller than that of GO by ~20 cm^{-1} (~115 cm^{-1} versus ~135 cm^{-1}). Such a fwhm decrease is commonly observed during GO reduction.[34] We simultaneously observe an increase in the I_D/I_G intensity ratio from 0.96 (GO) to 1.10 (rGO*) (Supplementary Figure S10), implying an increase in the average sp^2 dimension from 1.32 nm (GO) to 1.42 nm (rGO*). Domain sizes are estimated using the modified Tuinstra−Koenig relationship.[35,36] Corre-

dx.doi.org/10.1021/nl402057j | Nano Lett. XXXX, XXX, XXX−XXX

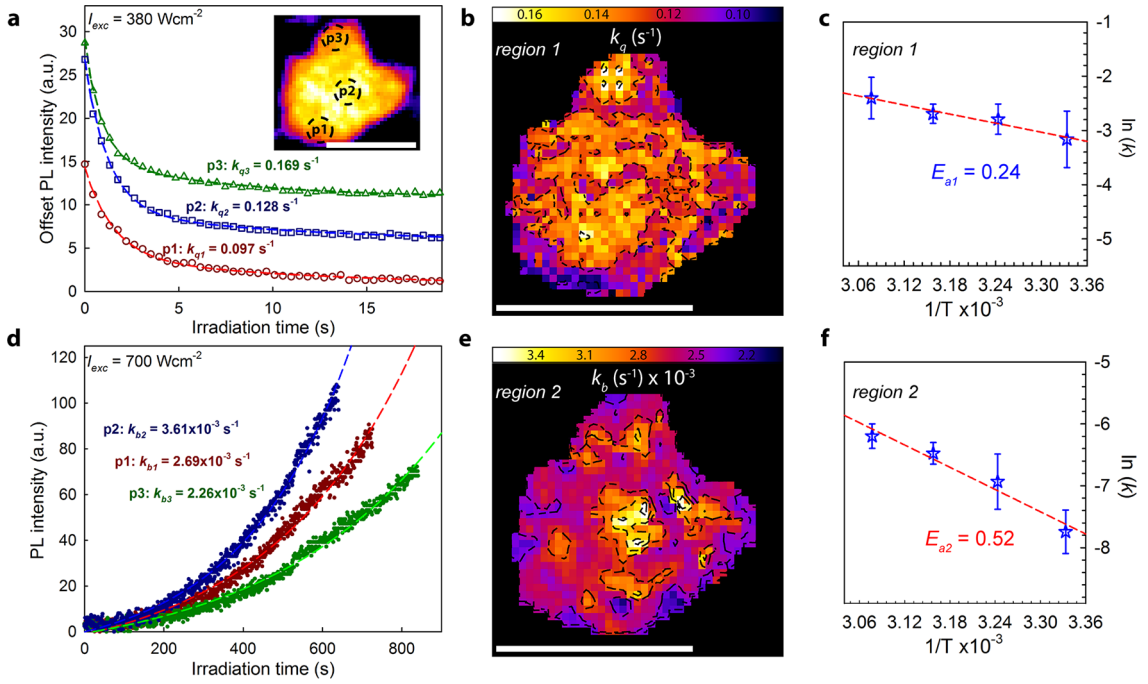

Figure 2. Heterogeneous reduction kinetics. Kinetic analysis of GO reduction (a–c, region 1) and rGO brightening (d–f, region 2). (a) Photoluminescence decay traces (open symbols) as a function of time for three different positions on a single GO sheet. Dashed lines represent corresponding biexponential fits. Extracted rate constants are k_q = 0.097 s^{-1}, 0.128 s^{-1}, and 0.169 s^{-1} for positions 1, 2, and 3, respectively. Traces offset for clarity. Inset: Time-averaged PL intensity with positions 1–3 ("p1", "p2", and "p3") marked using dashed circles. (b) Kinetic k_q map compiled from the photolytic reduction movie of a single GO sheet. Contour interval: 0.02 s^{-1}. (c) Arrhenius plot of GO reduction kinetics for temperatures between 298 and 323 K. Error bars indicate the standard deviation in k-values for five individual GO sheets at a given temperature. (d) Photobrightening traces as a function of time for the same 3 positions marked in the inset of a. Extracted k_b-values are 2.69 × 10^{-3} s^{-1}, 3.61 × 10^{-3} s^{-1}, and 2.26 × 10^{-3} s^{-1} for positions 1, 2, and 3, respectively. (e) k_b map (contour interval: 3 × 10^{-4} s^{-1}) and (f) Arrhenius plot of rGO brightening kinetics under identical conditions as in c. Scale bars: 5 μm.

sponding bandgaps (E_g) pre- and postbrightening [estimated using $E_g = (h\nu_F/2d)$, where h is Planck's constant, ν_F is the Fermi velocity, and d is the sp^2 domain size[9,37] (Supplementary Discussion S2)] are E_g = 2.64 eV and E_g = 2.46 eV. The predicted spectral redshift between GO to rGO* is therefore 180 meV and is in reasonable agreement with the 90 meV shift seen in Figure 1e.

Having correlated emission quenching/photobrightening with GO-to-rGO* interconversion, what remains is an explanation of the photobrightening effect between rGO and rGO* and, more importantly, a detailed mechanistic explanation of how GO is actually photoreduced. In this regard, GO photoreduction is commonly attributed to a photothermal effect.[20,38,39] The absorption of light causes local heating which, in turn, results in a temperature change that causes the desorption of oxygen containing functionalities. Corroborating this, temperature increases up to 500 °C have been reported in samples exposed to photographic flash lamps.[17]

Other studies, however, suggest photoreduction through the photolysis of oxygen containing functional groups in GO.[19,40,41] These species must therefore absorb light and require an electronic transition at or close to λ_{exc}. This is supported by highly oxidized ensemble GO absorption spectra in the literature, which show ligand-related $n\pi^*$ resonances between 400 and 420 nm.[40] Furthermore, recent PLE studies reveal striking structure in GO's visible excitation spectrum (between 400 and 550 nm), attributed to quasi-molecular ligand/sp^2 domain resonances.[29] These conclusions are consistent with recent TD-DFT studies which predict the existence of such transitions in the visible region.[28]

Following the absorption of light, either direct hydroxyl dissociation (binding energy, E_{bind} ~ 0.7 eV)[42] or C–O–C/C=O/COOH dissociation (E_{bind} > 1 eV)[19,40,43] occurs. Alternatively, photolysis induces oxygen containing functionalities to migrate across GO's basal plane. These migrating groups leave behind sp^2 hybridized carbons, localize at defect edges, and subsequently dissociate to form CO, CO_2, and H_2O/O_2.[19,40] Calculated OH and C–O–C migration activation energies are E_a ~ 0.32 eV and E_a ~ 0.9 eV, respectively.[19,44] Additional (more complicated) chemistries are also possible when multiple functional groups interact (mainly hydroxyls), giving rise to H_2O evolution. Associated activation energies range from E_a ~ 0.28–0.46 eV.[44] To summarize, possible photolytic processes are (from smaller to larger activation energies): OH migration (0.32 eV), multiple functional group reactions (0.28–0.46 eV), direct OH dissociation (0.7 eV), C–O–C migration (0.9 eV), and C–O–C/C=O/COOH dissociation (>1 eV). In all cases, slow photolytic reduction kinetics are predicted.

In our study, we discount a photothermal effect since employed laser intensities (I_{exc} ~ 380–700 W cm^{-2}) do not significantly heat individual GO sheets. This can be illustrated through an estimate of GO's temperature rise (ΔT) upon absorbing light.[45] Through $\Delta T \approx [(I_{exc}(1 - 10^{-A_\lambda}))/h]$, where A_λ is the absorbance at the excitation wavelength (A_λ = 0.0077)[21] and h is the interfacial thermal conductance between GO and air (or the substrate) [h_{air} ~ 1.0 × 10^5 W m^{-2} K^{-1} (h_{sub} ~ 5.0 × 10^7 W m^{-2} K^{-1})],[46] we find a maximum steady state ΔT rise of ~1 K. Resulting absolute temperatures are therefore far below the ~230 °C values typically required for thermal

dx.doi.org/10.1021/nl402057j | Nano Lett. XXXX, XXX, XXX–XXX

reduction.[21,47] Additional details about the calculation can be found in Supplementary Discussion S3.

To check on the photolytic reduction mechanism, wavelength-dependent studies have been conducted on single GO sheets by illuminating them with 522 and 640 nm light under identical conditions ($I_{exc} \sim 700$ W cm^{-2}, Supplementary Figure S11). In the case of 640 nm excitation, an initial emission decay characteristic of region 1 is essentially absent, with intensities decreasing only ~10% over the course of 30 min. Furthermore, no photobrightening characteristic of region 2 is seen. By contrast, experiments with 522 nm light show that individual GO sheets do quench/photobrighten, although much more slowly than in our default 405 nm experiments. These results can be rationalized since in the 640 nm case the frequency is off-resonance with any ligand-related transition. In the 522 nm case, the frequency is within the range of GO's ligand/sp^2 resonances between 400 and 550 nm,[29,28,40] enabling photolysis. This is also not completely unexpected since long wavelength photoreduction has previously been observed at the ensemble level.[21,48] We conclude that GO photoreduction is primarily photolytic in nature.

Dramatic movies illustrating GO's photolysis can be found in the Supporting Information. From them, we extract the kinetics and heterogeneity of the underlying (photolytic) chemistries occurring in regions 1 and 2. Figure 2a illustrates quenching trajectories taken from three different locations of a given GO sheet; positions are indicated in the inset. We see that position 1 decays slower than positions 2 and 3. These and other quenching traces are subsequently fit to exponential decays in order to obtain associated *reduction* rate constants, k_q. Empirically, we find that the quenching traces fit well to biexponential decays from where we report weighted (average) rate constants.[49] However, these fits are always dominated by the slow component (~70% relative contribution). In the case of positions 1, 2, and 3, we therefore find k_q-values of $k_{q1} = 0.097$ s^{-1}, $k_{q2} = 0.128$ s^{-1}, and $k_{q3} = 0.169$ s^{-1}. This suggests that electron migration cannot account for the observed photoreduction since an effective mobility of $\mu_{PL} \sim 6.1 \times 10^{-14}$ cm^2 V^{-1} s^{-1} is estimated from the above k_q-values (see Supplementary Discussion S4) and differs dramatically from reported rGO carrier mobilities (~10 cm^2 V^{-1} s^{-1}).[32]

To obtain a complete spatial map of GO's heterogeneous kinetics, we subsequently conduct an analysis where the rate constant for each pixel in a reduction movie is calculated. This is done using a home-written Java applet (source code, Supplementary Appendix S1). Figure 2b shows results from one such analysis, revealing a wide variance in k_q-values (from 0.085 s^{-1} to 0.17 s^{-1}). Through resulting rate constant maps, peaks (bright regions) and valleys (dark regions) in GO's spatial k_q distribution can be seen, highlighting its spatially heterogeneous reduction chemistries.

A similar analysis is conducted on brightening trajectories for the same positions of the same sheet. Given that prolonged illumination causes rGO* sheets to photobleach and that episodes of emission intermittency reminiscent of quantum dot blinking[50] accompany this process [trajectories and spectra are provided in the Supporting Information (S12)], our kinetic analysis only focuses on the initial brightening segment of photobrightening traces. Extracted kinetics are found to be first order with an exponential rise in PL with illumination time. Figure 2d illustrates obtained brightening rate constants (k_b), revealing $k_{b1} = 2.69 \times 10^{-3}$ s^{-1}, $k_{b2} = 3.61 \times 10^{-3}$ s^{-1}, and $k_{b3} = 2.26 \times 10^{-3}$ s^{-1} for positions 1, 2, and 3, respectively. The associated rate map [constructed using a similar Java applet (source code, Supplementary Appendix S2)] is shown in Figure 2e. Spatially heterogeneous kinetics are again observed, with a rate constant distribution ranging from ~1.9×10^{-3} s^{-1} to ~3.7×10^{-3} s^{-1}.

Interestingly, little correlation is observed between obtained k_q and k_b-values. For example, position 1 exhibits the smallest rate constant in region 1 ($k_{q1} < k_{q2} < k_{q3}$) but has a rate constant that lies between k_{b2} and k_{b3} in region 2 ($k_{b3} < k_{b1} < k_{b2}$). A comparison of the same sheet's quenching (Figure 2b) and brightening (Figure 2e) rate constant maps reveals this trend in more detail, highlighting differences in their spatially heterogeneous reduction/brightening kinetics. In general, we find no correlation between regions that quench quickly and those that brighten quickly. Consequently, this suggests that two distinct processes are responsible for the initial reduction of GO to rGO and its subsequent photobrightening to rGO*.

Finally, the above rate constants can be related to activation energies, E_a, by conducting temperature-dependent studies of GO reduction ($\lambda_{exc} = 405$ nm). When extracted k_q and k_b-values at different temperatures are graphed on an Arrhenius plot (Figure 2c,f), we find composite E_a values of $E_{a1} = 0.24$ eV (region 1) and $E_{a2} = 0.52$ eV (region 2). Upper and lower limits to these composite activation energies are E_{a1}~0.13−0.39 eV and E_{a2}~0.33−0.71 eV. Rate constants found in regions 1 and 2 of a given sheet (Figure 2) are therefore associated with activation energies that span E_{a1}= 0.20−0.22 eV ($k_q \sim 0.17$−0.085 s^{-1}) and $E_{a2} = 0.47$−0.50 eV ($k_b \sim 2.5 \times 10^{-3}$ to 1.0×10^{-3} s^{-1}).

Having established the energetics of processes in regions 1 and 2, we now provide a more definite physical and mechanistic picture of GO photoreduction. Specifically, the extracted photolysis E_a-values ($E_{a1} \sim 0.24$ eV) in region 1 suggest that this phase of reduction is dominated by OH migration due to its lower migration activation energies of 0.32 eV.[19,42,44] Hydroxyl groups migrate across the basal plane and subsequently localize in areas of high defect density.[44] Highly localized functional group concentrations then give rise to multiple functional group interactions (such as OH/OH and OH/C−O−C reactions), evolving H_2O in the process. Corresponding E_a-values for these processes range from 0.28 to 0.46 eV.[44] Consequently, little carbon is lost in this stage, and what results is rGO where fast nonradiative relaxation pathways induce an emission quenching and spectral blueshift.[27]

Next, the larger activation energies of region 2 ($E_{a2} \sim 0.52$ eV) are more consistent with direct OH dissociation (0.7 eV), C−O−C migration ($E_a \sim 0.9$ eV), or possibly C−O−C/C═O/COOH dissociation (>1 eV).[19,40,44] In all cases, photolysis of these functionalities results in significant carbon loss through CO and CO_2 evolution as seen in GO photolysis/mass spectrometry studies.[43,51] While this process is mainly destructive, a slight expansion of the average sp^2 domain size occurs. The resulting structure therefore resembles a loosely connected network of semi-isolated ligand/sp^2 domains. Loss of connecting carbons simultaneously means that nonradiative recombination pathways responsible for the quenching and blueshift of sp^2 domain emission are removed. This results in red emission and explains the apparent redshift as well as emission enhancement/intermittency in rGO*. Continued photolysis eventually destroys the sheets (Supplementary, Figure S4).[41] Along the same lines, continued irradiation causes isolated molecular-like sp^2 domains to photobleach.

dx.doi.org/10.1021/nl402057j | Nano Lett. XXXX, XXX, XXX−XXX

At this point, we construct vector field maps to capture the spatial/temporal evolution of GO photoreduction (source code, Supplementary Appendix S3). These vector field maps depict the direction and progression of GO's intrasheet reduction and subsequent photobrightening. Namely, they reveal where reduction (photobrightening) begins and how it flows across GO's basal plane, reproducing visual trends observed during photolysis movies.

Figure 3a shows one such reduction vector field map superimposed atop the same sheet's corresponding k_q rate

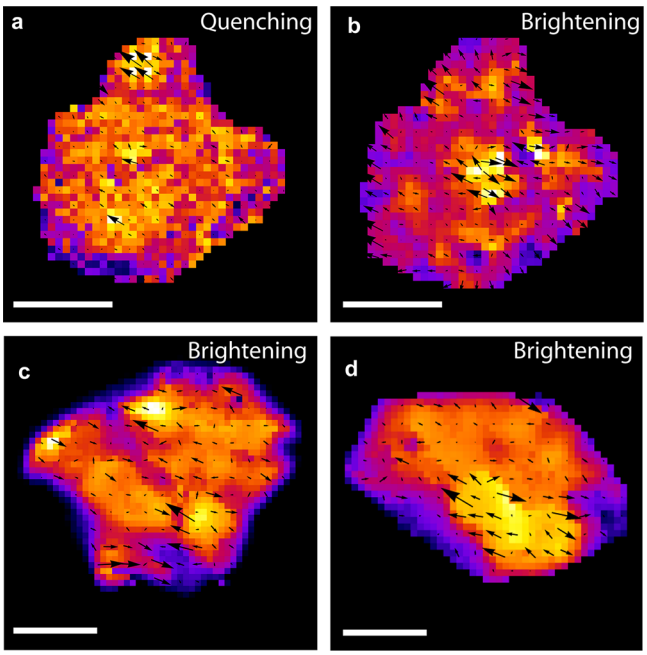

Figure 3. Single layer GO reduction dynamics. (a) Reduction vector field map of the GO sheet featured in Figure 2 superimposed atop its false color k_q rate map. Arrows show the velocity of the reduction front. Bright regions correspond to peaks in the underlying rate constant map. (b) Vector field map for the same sheet's PL enhancement phase, where bright regions again correspond to peaks in the underlying k_b map and arrows show the velocity of the brightening front. (c and d) Vector field and associated brightening rate maps of other GO sheets. Scale bars: 2.5 μm.

constant map. The figure reveals a direct correlation between peaks in the rate constant map and the spatial origin of GO reduction. This is seen in all vector field images (e.g., Figure 3a and Supplementary Figure S13). Likewise, a photobrightening vector field map for the same sheet shows a pronounced correlation between its rate constant peaks and the spatial origin of basal plane photobrightening (Figure 3b). In this regard, we have previously established that peaks in the k_b rate constant map correspond to native, red-emitting regions of rGO prior to photobrightening (Figure 1d). Vector field images for other GO sheets show similar trends (Figure 3c–d).

To explain the origin of a reduction/quenching front, we posit that areas with large local OH and defect concentrations quench first due to the dissociation of OH groups through multiple group photolytic processes having favorable E_a values.[44] In parallel, hydroxyl groups migrate to defect centers and subsequently react with surrounding functional groups through the same mechanism. Loss of H_2O through these processes rationalizes previous ensemble XPS and FTIR observations. Photolytic migration/dissociation continues until the local OH concentration is depleted, resulting in a network of interconnected sp^2 domains. This rationalizes how a reduction/quenching front propagates away from apparent nucleation points within GO's basal plane.

Next, we explain how subsequent photolysis propagates in region 2 upon prolonged illumination. Here, we have seen that red-emitting regions consisting of sp^2 domains that are nominally decoupled from an interconnected graphitic network are the first to brighten. Furthermore, an earlier thermal analysis has shown that steady state temperature changes in GO are proportional to the amount of light absorbed and to local thermal conductivities. As a consequence, ΔT differences as large as ~4 K can exist locally between highly absorptive/decoupled parts of the sheet and nearby semioxidized regions (Supplementary Discussion S3). While not enough to induce direct thermal dissociation, this temperature difference can significantly enhance the observed photobrightening kinetics associated with continued photolysis. To illustrate, a ~21% difference in brightening rates exists between a decoupled/reduced region and nearby regions within rGO's basal plane when E_a = 0.52 eV. Differences as large as 45% are possible when E_a = 0.70 eV (Supplementary Discussion S5). Experimentally, rate constant differences of ~15–40% are readily seen in Figure 2e between k_b peaks and neighboring regions, supporting the hypothesis. As a consequence, once photolysis/photobrightening begins in a region with strongly absorptive and decoupled sp^2 domains, oxygen-containing functional groups nearest to these domains experience temperature changes that enhance their photolytic dissociation rates. A photolysis/increased absorption/ΔT feedback loop then ensues, causing photolysis to propagate. This leads to photobrightening and, ultimately, to the continued reduction/eventual destruction of rGO.

To summarize, we have shown for the first time the direct observation of GO reduction through the light-induced photolysis of GO's oxygen containing functional groups. At the single sheet level, photolytic reduction is characterized by a quenching and blueshift of the emission. GO reduction arises from the photoinduced migration and subsequent dissociation of hydroxyl groups within its basal plane. Following reduction, rGO photobrightens. This phenomenon is attributed to fragmentation of as-produced sp^2 domains within an extended/interconnected network due to the photolytic removal of carbon containing species. Temperature gradients caused by thermal conductivity differences between decoupled and coupled regions in rGO's basal plane then seed additional photolytic events. This causes the photolysis to propagate. All experimental observations—the initial quenching/blueshifting, rGO's subsequent photobrightening/redshifting, ensemble absorption/XPS/FTIR data, single sheet kinetic rate maps, and associated activation energies—support this. In turn, these results reveal, in unprecedented detail, mechanistic aspects of GO's photoreduction and simultaneously provide a foundation for developing new strategies to spatially control its reduction.

Methods. *Synthesis of Graphene Oxide.* GO was prepared using a modified Hummers synthesis followed by sonochemical irradiation to disperse the sample. In a typical preparation, 300 mg of graphite, 36 mL of H_2SO_4, and 4 mL of H_3PO_4 were continuously stirred in an ice bath for 4 h. Afterward, 3.6 mg of $KMnO_4$ was added to the mixture, and the solution was stirred for another 48 h while ensuring that its temperature did not exceed 25 °C. The partially oxidized/exfoliated graphite was then diluted with deionized water to double the volume. This

dx.doi.org/10.1021/nl402057j | Nano Lett. XXXX, XXX, XXX–XXX

was followed by sonotrode sonication at 20 kHz for 1.5 h. To complete the preparation, 3% H_2O_2 was added to the suspension until it turned yellow, indicating a high degree of graphite oxidation. The suspension was centrifuged, washed with 1 M HCl, and repeatedly washed with DI water until a reddish brown suspension was obtained. GO samples were then freeze-dried, yielding a cream colored solid.

Ensemble Characterization. Ensemble samples were prepared by suspending solid GO samples in water and sonicating the suspension at 42 kHz for ∼10 s. rGO samples were then obtained by irradiating GO suspensions with 405 nm light (I_{exc} = 0.2 W cm^{-2}, 990 min). XPS measurements (ULVAC-PHI) were performed by depositing a thin film from these suspensions onto SiO_2 substrates. The absorbance of GO samples was measured using a Cary 50 Bio spectrometer following intervals of 405 nm irradiation. Transport measurements were carried out by drop-casting GO sheets onto glass substrates. Gold was then sputtered over the GO film, using a ∼60 μm shadow mask to create electrodes. Transport measurements were taken before and after 75 and 990 min of 405 nm irradiation (I_{exc} = 0.2 W cm^{-2} both cases).

Single Sheet Microscopy. Dilute solutions of GO suspended in ethanol and sonicated at 42 kHz for ∼10 s were drop-cast onto flamed fused silica microscope coverslips. An inverted optical microscope (Nikon) along with a continuous wave 405 nm (alternatively, 522 and 640 nm) laser (Coherent) was used to image individual sheets. The excitation was focused with a microscope objective (Zeiss, 1.4 N.A.) with emitted light collected using the same objective. The emission was passed through a 425 nm long pass filter (Thorlabs) to prevent any incident laser light from reaching the detectors.

Reduction experiments were performed using a wide-field illumination spot with an associated excitation intensity of I_{exc} ∼ 380 W cm^{-2} or 700 W cm^{-2}. In these experiments, a 30 cm focal length achromatic doublet was placed prior to the objective's back aperture to create a large (d ∼ 30 μm) excitation spot. A thermoelectrically cooled charge-coupled device (EM-CCD) (Andor) was used to collect the emission, which was then saved in multipage TIFF format. Integrated emission intensity trajectories were subsequently extracted using ImageJ. Rate maps of individual GO sheets were obtained using a home-written Java applet. Vector plots were also generated using a home-written Java applet. Single sheet PL spectra were acquired using 405 nm excitation (I_{exc} ∼ 380 W cm^{-2}) with the emitted light dispersed and collected with a spectrometer/EM-CCD combination (Acton; 50 grooves/mm, 600 nm blaze). Raman spectra were recorded using the same home-built microscope (λ_{exc} = 532 nm, I_{exc} ∼ 25 W cm^{-2}) with scattered light passed through a spectrometer (Acton; 300 grooves/mm, 700 nm blaze) and onto the EM-CCD. All spectra were corrected for the spectral response of the grating and the detector. Temperature-dependent studies entailed heating samples with a resistive element and controlling the temperature with a commercial temperature controller (Lakeshore).

2D PL maps of GO were acquired using a diffraction-limited focus, 405 nm excitation (I_{exc} ∼ 150 W cm^{-2}), two avalanche photodiodes (APDs, Perkin-Elmer), and a piezo stage (Mad City Laboratories) to move the sample relative to the excitation spot. The collected PL was then split using a broadband 50/50 beamsplitter (Chroma) with one beam passing through a 560 nm band-pass filter (Semrock) and the other through a 730 nm band-pass filter (Chroma). Ratio maps of GO sheets were constructed by dividing the 2D images in ImageJ. A schematic of the experimental setup used in single GO sheet PL measurements can be found in the Supporting Information (Figure S14).

■ ASSOCIATED CONTENT

Ⓢ Supporting Information

Photolysis movies; TEM micrographs; XPS spectra; fluorescence quenching microscopy images; reflectance contrast images of GO; additional emission ratio maps; quantum yield calculation details; ensemble absorption spectra; CI calculated absorption/emission spectra of carboxyl-functionalized aromatic clusters; FTIR spectra; transport measurements; single GO/rGO* sheet Raman spectra; band gap estimation calculation details; ΔT calculation details; excitation wavelength-dependent photolysis traces; effective mobility calculation details; Java applet source code; blinking trajectory/spectra; additional vector maps; PL setup schematic. This material is available free of charge via the Internet at http://pubs.acs.org.

■ AUTHOR INFORMATION

Corresponding Author

*E-mail: mkuno@nd.edu.

Author Contributions

M.P.M. and A.E. contributed equally. M.P.M. and A.E. performed the experiments. M.P.M. was responsible for all ensemble studies as well as single sheet PL spectral measurements, while A.E. was responsible for all other single sheet measurements. M.P.M., A.E., F.V., Y.M., D.A.S., J.H.H., P.V.K., and M.K. analyzed and interpreted the results. K.V. contributed GO samples. A.E., M.P.M., F.V., and J.T. set up the experiments. M.P.M., A.E., and M.K. cowrote the paper.

Notes

The authors declare no competing financial interest.

■ ACKNOWLEDGMENTS

We thank the ACS PRF (Type ND 51675, M.K. and P.V.K.), the Army Research Office (W911NF-12-1-0578, M.K.), the NSF (CREST, HRD-0833184, K.V.), NASA (URC, NNX09AV07A, K.V.), CONICET for international cooperation funds [D979(25-03-2013), J.H.H.], FONCyT (P.BID2009 PICTPRH107, J.H.H.), and the Department of Energy, Office of Basic Energy Sciences for financial support. We thank Sachidananda Krishnamurthy for aid with the TEM measurements. This is NDRL-4974 from the Notre Dame Radiation Laboratory, supported by the Division of Chemical Sciences, Geosciences, and Biosciences, Office of Basic Energy Sciences of the U.S. Department of Energy.

■ REFERENCES

(1) Novoselov, K. S.; Geim, A. K.; Morozov, S. V.; Jiang, D.; Katsnelson, M. I.; Grigorieva, I. V.; Dubonos, S. V.; Firsov, A. A. *Nature* **2005**, *438*, 197−200.

(2) Novoselov, K. S.; Jiang, Z.; Zhang, Y.; Morozov, S. V.; Stormer, H. L.; Zeitler, U.; Maan, J. C.; Boebinger, G. S.; Kim, P.; Geim, A. K. *Science* **2007**, *315*, 1379−1379.

(3) Katsnelson, M. I.; Novoselov, K. S.; Geim, A. K. *Nat. Phys.* **2006**, *2*, 620−625.

(4) Zhu, Y.; Murali, S.; Cai, W.; Li, X.; Suk, J. W.; Potts, J. R.; Ruoff, R. S. *Adv. Mater.* **2010**, *22*, 3906−3924.

(5) Luo, Z.; Vora, P. M.; Mele, E. J.; Johnson, A. T. C.; Kikkawa, J. M. *Appl. Phys. Lett.* **2009**, *94*, 111909-1−111909-3.

(6) Yan, J.-A.; Xian, L.; Chou, M. Y. *Phys. Rev. Lett.* **2009**, *103*, 086802-1−086802-4.
(7) Eda, G.; Mattevi, C.; Yamaguchi, H.; Kim, H.; Chhowalla, M. *J. Phys. Chem. C* **2009**, *113*, 15768−15771.
(8) Gómez-Navarro, C.; Weitz, R. T.; Bittner, A. M.; Scolari, M.; Mews, A.; Burghard, M.; Kern, K. *Nano Lett.* **2007**, *7*, 3499−3503.
(9) Gokus, T.; Nair, R. R.; Bonetti, A.; Bohmler, M.; Lombardo, A.; Novoselov, K. S.; Geim, A. K.; Ferrari, A. C.; Hartschuh, A. *ACS Nano* **2009**, *3*, 3963−3968.
(10) Stankovich, S.; Dikin, D. A.; Piner, R. D.; Kohlhass, K. A.; Kleinhammes, A.; Jia, Y.; Wu, Y.; Nguyen, S. T.; Ruoff, R. S. *Carbon* **2007**, *45*, 1558−1565.
(11) Li, D.; Müller, M. B.; Gilje, S.; Kaner, R. B.; Wallace, G. G. *Nat. Nanotechnol.* **2008**, *3*, 101−105.
(12) Gao, W.; Alemany, L. B.; Ci, L.; Ajayan, P. M. *Nat. Chem.* **2009**, *1*, 403−408.
(13) Loh, K. P.; Bao, Q.; Eda, G.; Chhowalla, M. *Nat. Chem.* **2010**, *2*, 1015−1024.
(14) Wang, X.; Zhi, L.; Müllen, K. *Nano Lett.* **2008**, *8*, 323−327.
(15) McAllister, M. J.; Li, J.-L.; Adamson, D. H.; Schniepp, H. C.; Abdala, A. A.; Liu, J.; Herrera-Alonso, M.; Milius, D. L.; Car, R.; Prud'homme, R. K.; Aksay, I. A. *Chem. Mater.* **2007**, *19*, 4396−4404.
(16) Li, X.; Zhang, G.; Bai, X.; Sun, X.; Wang, X.; Wang, E.; Dai, H. *Nat. Nanotechnol.* **2008**, *3*, 538−542.
(17) Gilje, S.; Dubin, S.; Badakshan, A.; Farrar, J.; Dansczyk, S. A.; Kaner, R. B. *Adv. Mater.* **2010**, *22*, 419−423.
(18) Williams, G.; Seger, B.; Kamat, P. V. *ACS Nano* **2008**, *2*, 1487−1491.
(19) Plotnikov, V. G.; Smirnov, V. A.; Alfimov, M. V.; Shul'ga, Y. M. *High Energy Chem.* **2011**, *45*, 411−415.
(20) Sokolov, D. A.; Shepperd, K. R.; Orlando, T. M. *J. Phys. Chem. Lett.* **2010**, *1*, 2633−2636.
(21) Zhou, Y.; Bao, Q.; Varghese, B.; Tang, L. A. L.; Tan, C. K.; Sow, C.-H.; Loh, K. P. *Adv. Mater.* **2010**, *22*, 67−71.
(22) Park, S.; Ruoff, R. S. *Nat. Nanotechnol.* **2009**, *4*, 217−224.
(23) Dreyer, D. R.; Park, S.; Bielawski, C. W.; Ruoff, R. S. *Chem. Soc. Rev.* **2010**, *39*, 228−240.
(24) Paci, J. T.; Belytschko, T.; Schatz, G. C. *J. Phys. Chem. C* **2007**, *111*, 18099−18111.
(25) Hummers, W. S.; Offeman, R. E. *J. Am. Chem. Soc.* **1958**, *80*, 1339−1339.
(26) Kim, J.; Cote, L. J.; Kim, F.; Huang, J. *J. Am. Chem. Soc.* **2010**, *132*, 260−267.
(27) Exarhos, A. L.; Turk, M. E.; Kikkawa, J. M. *Nano Lett.* **2013**, *13*, 344−349.
(28) Chien, C.-T.; Li, S.-S.; Lai, W.-J.; Yeh, Y.-C.; Chen, H.-A.; Chen, I.-S.; Chen, L.-C.; Chen, K.-H.; Nemoto, T.; Isoda, S.; Chen, M.; Fujita, T.; Eda, G.; Yamaguchi, H.; Chhowalla, M.; Chen, C.-W. *Angew. Chem., Int. Ed.* **2012**, *51*, 6662−6666.
(29) Galande, C.; Mohite, A. D.; Naumov, A. V.; Gao, W.; Ci, L.; Ajayan, A.; Gao, H.; Srivastava, A.; Weisman, R. B.; Ajayan, P. M. *Sci. Rep.* **2011**, *1*, 1−5.
(30) Mak, K. F.; Ju, L.; Wang, F.; Heinz, T. F. *Solid State Commun.* **2012**, *152*, 1341−1349.
(31) Eda, G.; Fanchini, G.; Chhowalla, M. *Nat. Nanotechnol.* **2008**, *3*, 270−274.
(32) Eda, G.; Lin, Y.-Y.; Mattevi, C.; Yamaguchi, H.; Chen, H.-A.; Chen, I.-S.; Chen, C.-W.; Chhowalla, M. *Adv. Mater.* **2010**, *22*, 505−509.
(33) Schmidt, M. W.; Baldridge, K. K.; Boatz, J. A.; Elbert, S. T.; Gordon, M. S.; Jensen, J. H.; Koseki, S.; Matsunaga, N.; Nguyen, K. A.; Su, S.; Windus, T. L.; Dupuis, M.; Montgomery, J. A. *J. Comput. Chem.* **1993**, *14*, 1347−1363.
(34) Petridis, C.; Lin, Y.-H.; Sawa, K.; Eda, G.; Kymakis, E.; Anthopoulos, T. D.; Stratakis, E. *Appl. Phys. Lett.* **2013**, *102*, 093115-1−093115-5.
(35) Tuinstra, F.; Koenig, J. L. *J. Chem. Phys.* **1970**, *53*, 1126−1130.
(36) Ferrari, A. C.; Robertson, J. *Phys. Rev. B* **2000**, *61*, 14095−14107.
(37) Geim, A. K.; Novoselov, K. S. *Nat. Mater.* **2007**, *6*, 183−191.
(38) Matsumoto, Y.; Koinuma, M.; Kim, S. Y.; Wantanabe, Y.; Taniguchi, T.; Hatakeyama, K.; Tateishi, H.; Ida, S. *ACS Appl. Mater. Interfaces* **2010**, *2*, 3461−3466.
(39) Cote, L. J.; Cruz-Silva, R.; Huang, J. *J. Am. Chem. Soc.* **2009**, *131*, 11027−11032.
(40) Andryushina, N. S.; Stroyuk, O. L.; Dudarenko, G. V.; Kuchmiy, S. Y.; Pokhodenko, V. D. *J. Photochem. Photobiol., A* **2013**, *256*, 1−6.
(41) Matsumoto, Y.; Koinuma, M.; Ida, S.; Hayami, S.; Taniguchi, T.; Hatakeyama, K.; Tateishi, H.; Wantanabe, Y.; Amano, S. *J. Phys. Chem. C* **2011**, *115*, 19280−19286.
(42) Lahaye, R. J. W. E.; Jeong, H. K.; Park, C. Y.; Lee, Y. H. *Phys. Rev. B* **2009**, *79*, 125435-1−125435-8.
(43) Smirnov, V. A.; Shul'ga, Y. M.; Denisov, N. N.; Kresova, E. I.; Shul'ga, N. Y. *Nanotechnol. Russ.* **2012**, *7*, 156−163.
(44) Ghaderi, N.; Peressi, M. *J. Phys. Chem. C* **2010**, *114*, 21625−21630.
(45) Wang, D.; Carlson, M. T.; Richardson, H. H. *ACS Nano* **2011**, *5*, 7391−7396.
(46) Cai, W.; Moore, A. L.; Zhu, Y.; Li, X.; Chen, S.; Shi, L.; Ruoff, R. S. *Nano Lett.* **2010**, *10*, 1645−1651.
(47) Jeong, H.-K.; Lee, Y. P.; Jin, M. H.; Kim, E. S.; Bae, J. J.; Lee, Y. H. *Chem. Phys. Lett.* **2009**, *470*, 255−258.
(48) Zhang, Y.; Guo, L.; Wei, S.; He, Y.; Xia, H.; Chen, Q.; Sun, H.-B.; Xiao, F.-S. *Nano Today* **2010**, *5*, 15−20.
(49) Robel, I.; Bunker, B. A.; Kamat, P. V. *Adv. Mater.* **2005**, *17*, 2458−2463.
(50) Frantsuzov, P.; Kuno, M.; Janko, B.; Marcus, R. A. *Nat. Phys.* **2008**, *4*, 519−522.
(51) Shul'ga, Y. M.; Martynenko, V. M.; Muradyan, V. E.; Baskakov, S. A.; Smirnov, V. A.; Gutsev, G. L. *Chem. Phys. Lett.* **2010**, *498*, 287−291.